The Astrophysical Journal, 946:38 (14pp), 2023 March 20 https://doi.org/10.3847/1538-4357/acbf49

Do Hα Stokes *V* Profiles Probe the Chromospheric Magnetic Field? An Observational Perspective*

Harsh Mathur[1], K. Nagaraju[1], Jayant Joshi[1], and Jaime de la Cruz Rodríguez[2]
[1] Indian Institute of Astrophysics, II Block, Koramangala, Bengaluru 560 034, India
[2] Institute for Solar Physics, Department of Astronomy, Stockholm University, AlbaNova University Centre, SE-10691 Stockholm, Sweden
Received 2023 January 10; revised 2023 February 23; accepted 2023 February 24; published 2023 March 27

Abstract

We investigated the diagnostic potential of the Stokes *V* profile of the Hα line to probe the chromospheric line-of-sight (LOS) magnetic field ($B_{\rm LOS}$) by comparing the $B_{\rm LOS}$ inferred from the weak field approximation (WFA) with that inferred from the multiline inversions of the CaII 8542 Å, Si I 8536 Å, and Fe I 8538 Å lines using the STiC inversion code. Simultaneous spectropolarimetric observations of a pore in the Ca II 8542 Å and Hα spectral lines obtained from the SPINOR at the Dunn Solar Telescope on 2008 December 4 are used in this study. The WFA was applied on the Stokes *I* and *V* profiles of Hα line over three wavelength ranges, viz., around line core ($\Delta\lambda = \pm 0.35$ Å), line wings ($\Delta\lambda = [-1.5, -0.6]$, and $[+0.6, +1.5]$ Å), and full spectral range of the line ($\Delta\lambda = \pm 1.5$ Å) to derive the $B_{\rm LOS}$. We found the maximum $B_{\rm LOS}$ strengths of $\sim$+800 and $\sim$+600 G at $\log \tau_{500} = -1$ and −4.5, respectively, in the pore. The morphological map of the $B_{\rm LOS}$ inferred from the Hα line core is similar to the $B_{\rm LOS}$ map at $\log \tau_{500} = -4.5$ inferred from multiline inversions. The $B_{\rm LOS}$ map inferred from the Hα line wings and full spectral range have a similar morphological structure to the $B_{\rm LOS}$ map inferred at $\log \tau_{500} = -1$. The $B_{\rm LOS}$ estimated from Hα using WFA is weaker by a factor of ≈0.53 than that of inferred from the multiline inversions.

Unified Astronomy Thesaurus concepts: Spectropolarimetry (1973); Radiative transfer (1335); Solar chromosphere (1479); Solar magnetic fields (1503)

1. Introduction

Between the bright solar surface and the million degrees hot corona, the chromosphere is one of the most dynamic and complex layers of the solar atmosphere. Understanding the magnetic coupling of the chromosphere with the photosphere, transition region, and corona may reveal how mass and energy are supplied to the corona and heliosphere. Therefore, simultaneous magnetic field measurements at multiple heights of the solar atmosphere are important.

Magnetic field measurements in the photosphere are routinely made, and significant progress has been made in the techniques that allow for chromospheric magnetic field measurements. The most widely used lines to probe the magnetic field of the solar chromosphere are the Ca II 8542 Å and He I 10830 Å lines (Lagg et al. 2017). While using these lines to probe the chromospheric magnetic field has its advantages, like the relatively well-understood line formation, and they can be interpreted utilizing nonlocal thermodynamic equilibrium (non-LTE) inversion codes (e.g., Socas-Navarro et al. 2000a; Asensio Ramos et al. 2008; de la Cruz Rodríguez et al. 2016, 2019; Ruiz Cobo et al. 2022), they also have some limitations. The He I 10830 Å line forms in a narrow range of heights in the upper chromosphere and line formation depends on coronal and transition region EUV radiation (Andretta & Jones 1997; Leenaarts et al. 2016). The Ca II 8542 Å line forms from the upper photosphere to the mid-chromosphere, however, the Ca II ion gets ionized to the Ca III ion in flaring regions, and hence the Ca II 8542 Å line itself may sample deeper layers of the solar atmosphere (Kerr et al. 2016; Kuridze et al. 2018; Bjørgen et al. 2019).

On the other hand, the Hα line seems to probe a relatively wider temperature range. Carlsson & Stein (2002) have shown that the Hα opacity in the upper chromosphere is determined by the ionization degree and radiation field. Using 3D radiative transfer calculations, Leenaarts et al. (2012a) have shown that ionization degree and the radiation field are insensitive to local temperature variations over time but are determined by mass density. More recently, Bjørgen et al. (2019) have also confirmed that the Hα line retains opacity even in flaring active regions by synthesizing spectra using a 3D rMHD simulation. Therefore, the Hα line always retains opacity in the chromosphere.

In spite of the diagnostic capabilities of the Hα line, very few spectropolarimetric observations have been reported in the literature. For example, Abdussamatov (1971) estimated vertical magnetic field gradient using simultaneous measurements of the Fe I 6302.5 Å and Hα lines. Simultaneous spectropolarimetric observations from the Hα line and lines of Fe I atom have been reported in the literature to compare the photospheric and chromospheric magnetic fields in sunspots (Balasubramaniam et al. 2004; Hanaoka 2005; Nagaraju et al. 2008). Radial variation of the line-of-sight magnetic field in the chromosphere and photosphere of a sunspot were discussed by Nagaraju et al. (2020a). Magnetic fields in prominences were diagnosed using spectropolarimetric observations of the Hα line (López Ariste et al. 2005). Jaume Bestard et al. (2022) studied linear and circular polarization signals near the north and south Solar Limb and inferred the LOS magnetic field using the weak field approximation (WFA).

* Not yet released.

The reason for so few spectropolarimetric observations of the Hα line have been reported and why this has not been a preferred line for the chromospheric magnetometry is because it is challenging to model the Hα line. Though the Stokes *V* signal is dominated by the Zeeman effect, both the intensity and polarization profiles of this line are sensitive to the 3D radiation field. Furthermore, in case of weakly magnetized atmospheres, the Stokes *Q* and *U* signals are sensitive to atomic polarization (Štěpán & Trujillo Bueno 2010, 2011), making this line difficult to model using the currently available inversion codes which adopt 1.5D plane-parallel geometry. It is also important to note that, in the weak field regime (when Zeeman Splitting, $\Delta\lambda_B$, is much smaller than the Doppler width, $\Delta\lambda_D$), the amplitude of circular polarization is proportional to the ratio of $\Delta\lambda_B$ to $\Delta\lambda_D$, and the linear polarization is proportional to the square of that ratio (for more details, see page 405 of Landi Degl'Innocenti & Landolfi 2004). This ratio, owing to the light weight of the hydrogen atom and thus correspondingly large Doppler width, is typically small compared to that in the case of heavier atoms like calcium.

In a study by Socas-Navarro & Uitenbroek (2004) who calculated 1D response functions of Stokes parameters of the Hα line and showed that it exhibits significant sensitivity to the photospheric magnetic fields in addition to the chromospheric magnetic fields. However, it has been shown by Leenaarts et al. (2012a) that 1D radiative transfer is not a good approximation to model the Hα line, treatment of radiative transfer in 3D is necessary. When the radiative transfer is treated in 3D, the Hα line traces the chromospheric magnetic features like fibrils, and it has been shown that it is a good chromospheric diagnostic. This finding is further supported by recent work by Bjørgen et al. (2019).

In this study, we explore the diagnostic potential of the Hα line to probe the chromospheric magnetic field using spectropolarimetric observations simultaneously recorded in the Hα and Ca II 8542 Å lines. We compare the magnetic field inferred using the WFA method on the Stokes *I* and *V* profiles of the Hα spectral line with the stratification (from the photosphere to the chromosphere) of line-of-sight (LOS) magnetic field inferred using the inversions of the Ca II 8542 Å line using a non-LTE inversion code.

2. Observations

The observations were made with the Spectro-Polarimeter for Infrared and Optical Regions (SPINOR: Socas-Navarro et al. 2006) instrument at the Dunn Solar Telescope (Dunn 1969) at the Sacramento Peak Observatory in the Hα and Ca II 8542 Å lines simultaneously. The Fe I 6569 Å line was recorded in the Hα spectrum and the Si I 8536 Å and Fe I 8538 Å lines were recorded in the Ca II 8542 Å spectrum. The spectral sampling of the Hα and Ca II 8542 Å lines data are 22 mÅ and 33 mÅ, respectively. The pixel scale corresponds to ∼0.″38 on the solar surface along the slit. The observed field of view (FOV) consists of a pore centered at north 28.°3 and east 16.°7 in the Stonyhurst heliographic coordinates system on 2008 December 4, starting at 15:35 UT with a viewing angle $\cos\theta = \mu = 0.8$. Here, θ is the angle between the LOS direction and the local surface normal. Twenty spectropolarimetric raster scans of 20 slit positions with a step size of 0.″375 were recorded; however, only four scans had good seeing conditions, and only the first scan is used in this study. Adaptive optics (AO; Rimmele 2000) were used during the observations. The data were corrected for dark- and flat-field variations and instrumental polarization. The details are given in Appendix A. In spite of strictly simultaneous observations, there was a spatial shift, due to atmospheric refraction, between the images at these two wavelengths, which were taken care of by co-aligning the Hα data with the Ca II 8542 Å data by cross-correlating the far-wing images of the Hα and Ca II 8542 Å lines. The signal-to-noise ratio (SNR) in the Hα data is higher (5×10^3) than in the Ca II 8542 Å data (10^3).

An overview of observations is shown in Figure 1. A pore almost centrally located in the FOV can be seen in the far-wing images of the Ca II 8542 Å and Hα lines (see panels (a) and (b) of Figure 1). The pore morphologically has a different shape in the Ca II 8542 Å and Hα lines and is brighter in the Hα line core image (see panels (c) and (d) of Figure 1). Panels (e) and (f) show the LOS magnetic field (B_{LOS}) inferred from the Ca II 8542 Å and Fe I 6569 Å lines, respectively. More details on the methods to infer the B_{LOS} are discussed in Section 3. There is an opposite polarity region near the pore visible in the photosphere that is absent in the WFA B_{LOS} map of the chromosphere.

The quiet-Sun profiles for the Hα and the Ca II 8542 Å lines were calculated by averaging profiles of a few pixels in a region away from the pore with negligible signal in the Stokes *V* profiles. As explained in Appendix A, the wavelength calibration was done by comparing the quiet-Sun profile with the BASS 2000 atlas profile. The Ca II 8542 Å and Hα data were also corrected for spectral veil.

In the following paragraphs, we discuss a few selected profiles that are chosen such that they show distinct features from one another corresponding to various dynamics observed in the FOV. In the top two panels of Figure 2, we present sample spectral images of Stokes *I* and *V* corresponding to a slit position marked by a brown line in Figure 1. In the bottom two panels of Figure 2, we show a few profiles from selected spatial locations marked using colored horizontal lines in the top two panels. The left and right columns of panels correspond to the Ca II 8542 Å and Hα spectrum, respectively.

There is a hint of enhancement in the intensity in the red wing of the Ca II 8542 Å line profile at 8542.38 Å ($\Delta v = +10.31$ km s^{-1}), at slit position near ∼4.″2 with the line core position (8542.04 Å) slightly blueshifted ($\Delta v = -1.5$ km s^{-1}) compared to the quiet-Sun profile (see violet-colored profile). The corresponding Hα profile shows nominal absorption. The violet-colored profile lies in the opposite polarity region. The Stokes *V* profiles of the Ca II 8542 Å and Hα lines have a weak signal with sign opposite to that of the Stokes *V* profile of the Fe I 6569 Å. There is hardly any signal in the Stokes *V* profile of the Si I 8536 Å and Fe I 8538 Å lines that is above the noise level. This is because, as noted above, the SNR in Ca II 8542 Å spectrum is about five times lower compared to that of Hα spectrum.

The intensity profile of the Ca II 8542 Å line at slit position near 7.″8 (blue-colored profile) shows emission in the blue wing at 8541.9 Å ($\Delta v = -6.56$ km s^{-1}) and line core (8542.12 Å) red-shifted ($\Delta v = +1.4$ km s^{-1}), signature of surge flow (more details are discussed in K. Nagaraju et al. 2023, in preparation). The corresponding Hα and the wings of Ca II 8542 Å intensity profiles also show red excursion compared to the quiet-Sun profile. The Stokes *V* profile of the Ca II 8542 Å line shows a sign reversal compared to the Stokes *V* profile of the Fe I 6569 Å, which is not due to change in the polarity of the magnetic field, but is due to

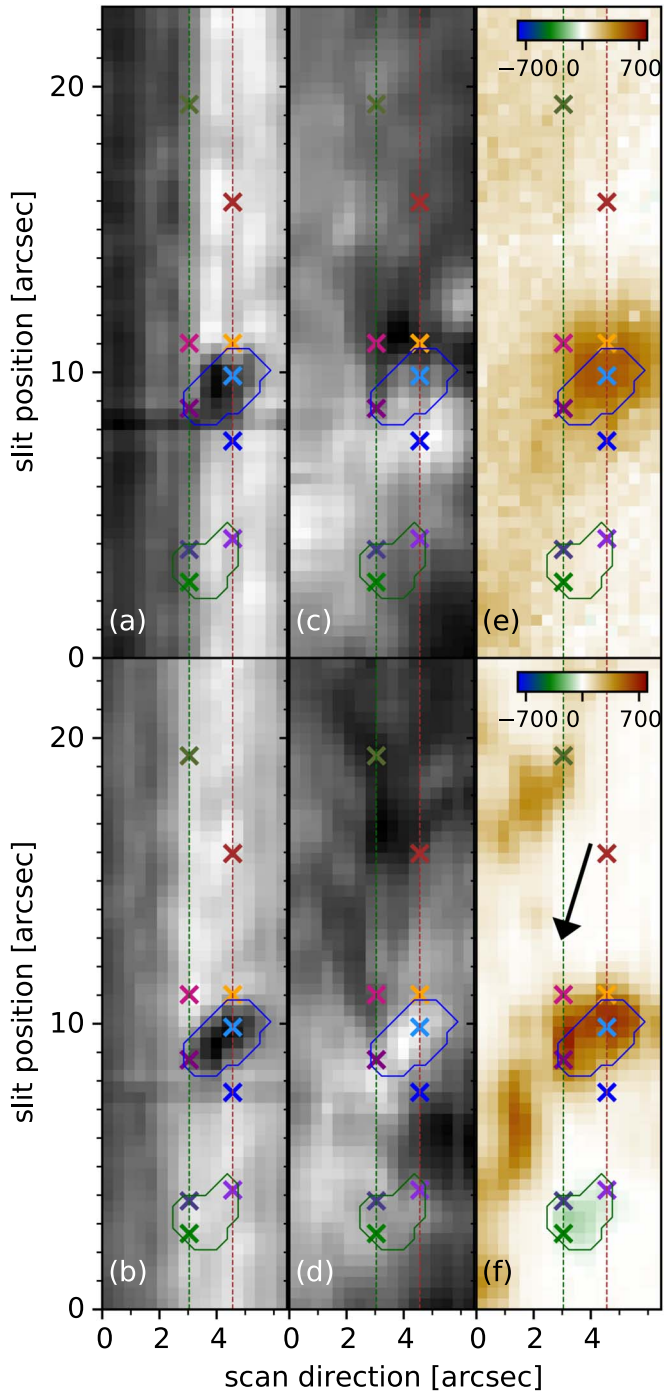

Figure 1. Field of view with a pore in the center as observed by the Dunn Solar Telescope on 2008 December 4: (a) far-wing image at an offset of −7 Å from the Ca II 8542 Å line, (b) far-wing image at an offset of +7 Å from the Hα line, (c) Ca II 8542 Å line core image, (d) Hα line core image. Panels (e) and (f) show LOS magnetic field maps derived under weak field approximation from the Ca II 8542 Å line within the spectral range of ±0.25 Å and Milne–Eddington inversions of the Fe I 6569 Å line, respectively. The blue contours show the location of the pore made using intensity thresholding on the far-wing image of Hα line in panel (b). The green contours show the location of the region with the negative polarity of the magnetic field seen in panel (f). The arrow indicates the disk-center direction.

emission in the blue wing (Sanchez Almeida 1997). Such an emission feature can only be caused by a change in the gradient of the source function, which also affects the sign of the Stokes *V* signal.

A sample profile over the pore is shown in cyan color. The Ca II 8542 Å and Hα lines show asymmetric Stokes *V* profiles with blue and red lobe amplitudes of (∼9%, ∼6%) and (∼1.3%, ∼0.9%), respectively. In contrast, the Si I 8536 Å, Fe I 8538 Å, and Fe I 6569 Å lines show relatively symmetric Stokes *V* profiles of amplitudes ∼1.6%, ∼1%, and ∼3.5%, respectively.

There is a hint of enhancement in the red wing of the Ca II 8542 Å line profile at the edge of the pore (yellow-colored profile). The Stokes *V* profiles of the Ca II 8542 Å and Hα lines (similar to cyan-colored profile) show amplitude asymmetry. This could be because of the presence of multiple Stokes components within one resolution element (Socas-Navarro et al. 2000b) or gradients in LOS velocity and magnetic field (Sankarasubramanian & Rimmele 2002).

The brown-colored profile is an example of a quiescent profile away from the pore region. The Stokes *V* amplitudes of the Ca II 8542 Å and Hα line profiles are similar (0.2%).

Figure 3 shows spectropolarimetric images and spectral profiles for the slit position shown in green color in Figure 1 which passes over a location with stronger field within the negative polarity region and the pore edge. The profiles over the negative polarity region are shown in green and purple colors. The Stokes *V* amplitudes of the Si I 8536 Å and Ca II 8542 Å lines are ∼0.7%. The green- and purple-colored intensity profiles of the Ca II 8542 Å line are blueshifted by about $\Delta\lambda = -0.04$ and -0.02 Å ($\Delta v = -1.4$ and 0.7 km s^{-1}), respectively, whereas there is no Doppler shift seen in the Si I 8536 Å and Fe I 8538 Å lines. The sign of the Stokes *V* profiles of the Si I 8536 Å, Fe I 8538 Å, and Fe I 6569 Å lines is opposite to that of the sign of the Stokes *V* profiles of the Ca II 8542 Å and Hα lines, which suggest that the Stokes *V* profile of the Hα line probes the chromospheric magnetic field. This most probably is because the Hα and Ca II 8542 Å line cores are sampling the canopy fields extending from a nearby region and overlying the opposite polarity region. To further demonstrate the existence of such field configuration, we show in Figure 4 sample spectral images and profiles of the same region but from a raster scan recorded at a later time (16:08 UT). As clearly seen in this figure, the sign of the Stokes *V* profiles corresponding to the core of Ca II 8542 Å and Hα lines are opposite to that of Stokes *V* profiles of the photospheric lines viz., Si I 8536 Å, Fe I 8538 Å, and Fe I 6569 Å (see spectral images from 2″ to 6″). On the other hand, the Stokes profiles in the wings of the Ca II 8542 Å and Hα lines show the polarity the same as that of the photospheric lines. This is consistent with the canopy field scenario as explained above since the line wings of Hα and Ca II 8542 Å lines form deeper in the solar atmosphere, and hence the Stokes *V* profiles have the same sign as that of the photospheric lines. However, as noted before, under weak field conditions, the Stokes *V* profiles change sign when the spectral features change from absorption to emission or vice-versa. In order to make sure that the change in sign of Stokes *V* profiles from core to wing of the chromospheric lines is actually because of the change in polarity of the magnetic field but not due to change in spectral features, we have over-plotted the first derivative of Stokes *I* ($\frac{dI}{d\lambda}$: the dotted green curves in the bottom panel of Figure 4 with the sign changed) over the Stokes *V* profiles. The reason for doing this is that, under weak field conditions, the Stokes *V* profile resembles $\frac{dI}{d\lambda}$ profile (see Section 3.1). The comparison

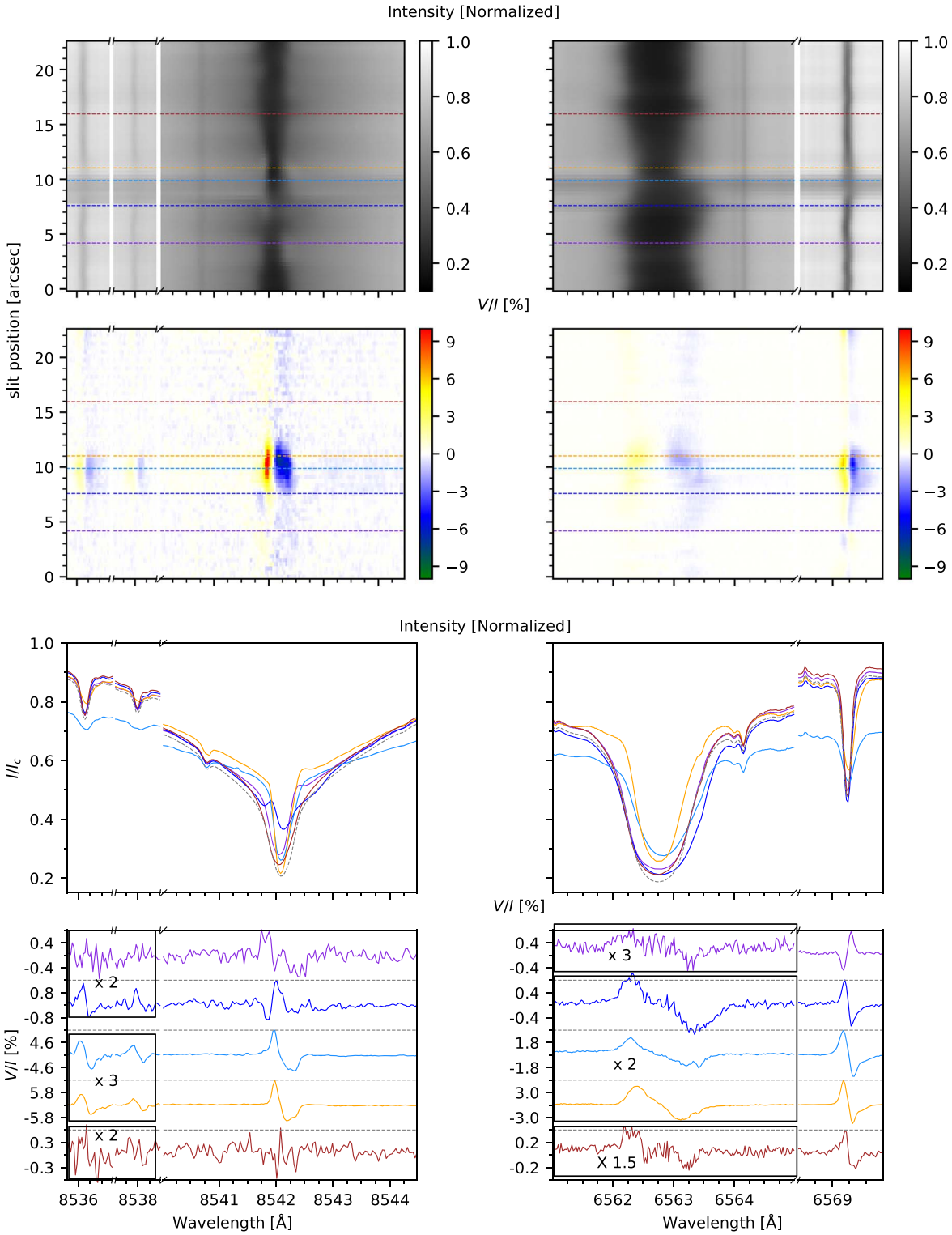

Figure 2. Sample Ca II 8542 Å and Hα line profiles over one slit position located over the pore and surrounding region (marked by the brown dashed line in Figure 1). The top two panels show the spectral images of Stokes *I* and *V*, respectively. A few selected profiles marked by colored dashed lines are plotted in the bottom two panels. The quiet-Sun profile (gray dashed) is also shown in the intensity plots for comparison. For better visibility, the amplitudes of a few Stokes *V* profiles are artificially multiplied by the factors as indicated in the respective panels.

between the Stokes *V* and $\frac{dI}{d\lambda}$ profiles clearly demonstrate that the Stokes *V* sign change from core to wings of the chromospheric lines is due to the change in the polarity of the magnetic field but not due to change in the emission or absorption features of Stokes *I*.

The profile shown in maroon (Figure 3) is another example of a profile in pore region. There is a red excursion in the Ca II 8542 Å line wings and Hα line core profile corresponding to a surge flow. The Stokes *V* profiles of the CaII 8542 Å, H α, and Fe I 6569 Å lines show amplitude asymmetry, and the blue

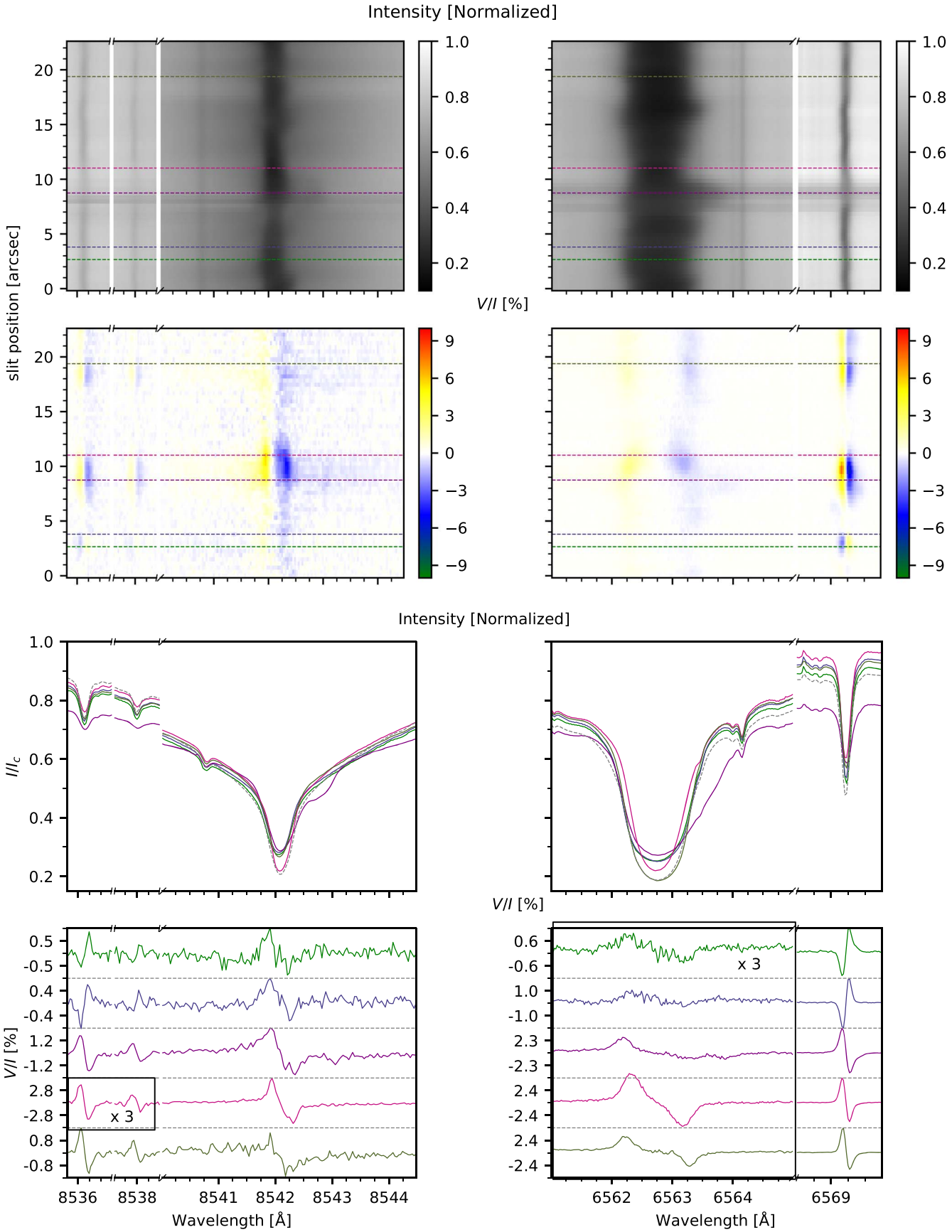

Figure 3. Same as Figure 2 but for the slit passing through the region over negative polarity seen in B_{LOS} map inferred from ME inversions (see green line in Figure 1).

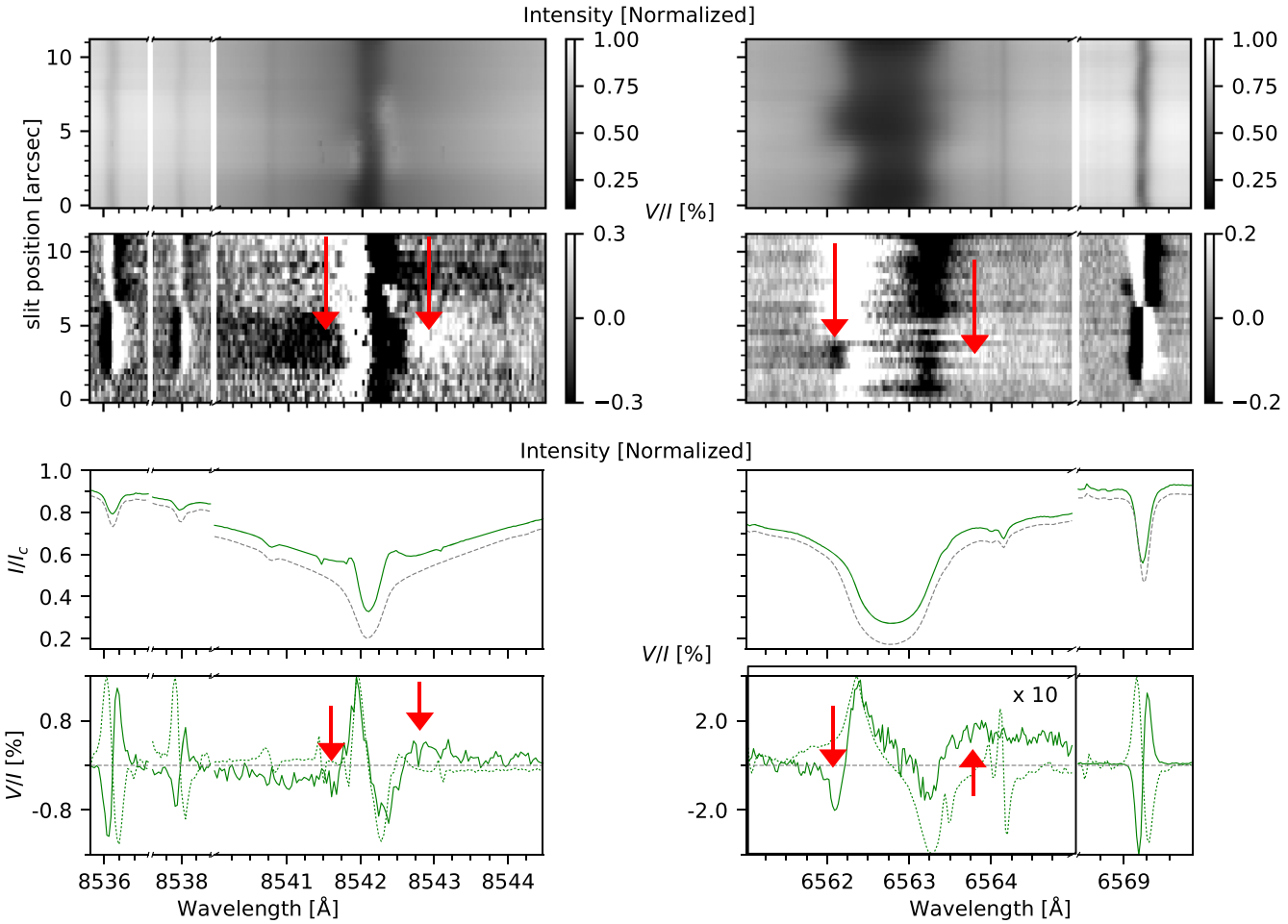

Figure 4. Sample Ca II 8542 Å and Hα line profiles over a region (in another raster scan map) with opposite polarity in the photospheric and chromospheric lines. The top two panels show the spectral images of Stokes *I* and *V*, respectively. An average Stokes *I* and *V* profile over the opposite polarity region is shown in the bottom two panels. The arrow indicates the wavelength position of the peak amplitude of the polarity reversal. The dotted green profile shows the derivative of Stokes *I* multiplied by −1. The quiet-Sun profile (gray dashed) is also shown in the intensity plots for comparison. For better visibility, the amplitudes of the Stokes *V* profile of the Hα line are artificially multiplied by the factors as indicated in the respective panel.

lobe show a positive sign suggesting positive polarity of the $B_{\rm LOS}$.

The pink and khaki-colored profiles show profiles away from the pore region. The intensity profiles of the Ca II 8542 Å and Hα lines are similar to that of the quiet-Sun profile. Amplitude asymmetry is present in the Stokes *V* profiles of the Ca II 8542 Å and Hα lines.

3. Methods

3.1. Weak Field Approximation

The magnetic field from the Hα spectral line was inferred using the weak field approximation (WFA). Under WFA, the Stokes *V* is linearly related to $B_{\rm LOS}$ and $(\partial I/\partial\lambda)$ through (Landi Degl'Innocenti & Landolfi 2004)

$$V(\lambda) = -\Delta\lambda_B\, \bar{g} \cos\theta\, \frac{\partial I}{\partial \lambda}, \tag{1}$$

and

$$\Delta\lambda_{\rm B} = 4.67 \times 10^{-13} \lambda_0^2 B, \tag{2}$$

where $\Delta\lambda_B$ is expressed in Å, *B* in Gauss, $\bar{g}$ is effective Landé factor, θ is the inclination of *B* with respect to the LOS, and λ_0 is the central wavelength of the spectral line (expressed in Å).

The $B_{\rm LOS}$ can be derived from Equation (1) using the linear regression formula (e.g., Martínez González & Bellot Rubio 2009),

$$B_{\rm LOS} = -\frac{\Sigma_\lambda \frac{\partial I_\lambda}{\partial\lambda} V(\lambda)}{C\Sigma_\lambda \left(\frac{\partial I_\lambda}{\partial\lambda}\right)^2}, \tag{3}$$

where $C = 4.66 \times 10^{-13}\, \bar{g}\, \lambda_0^2$.

We have used $\bar{g} = 1.048$ following the investigation done by Casini & Landi Degl'Innocenti (1994). We derived three values of $B_{\rm LOS}$, one from the line core (Hα $\pm$ 0.35 Å), the line wings ([−1.5, −0.6] and [+0.6, +1.5] Å), and over the full Hα spectral line (Hα $\pm$ 1.5 Å). The spectral blends listed in Table 1 were excluded while calculating $B_{\rm LOS}$ using the WFA, as have done by Jaume Bestard et al. (2022) and Nagaraju et al. (2020a). The WFA is applied on the Ca II 8542 Å line within the wavelength range $\lambda_0 \pm 0.25$ Å and the inferred $B_{\rm LOS}$ map is shown in panel (e) of Figure 1. The uncertainties in the values

Table 1
Removed spectral lines.

λ_0 (Å)	$\Delta\lambda_0$ (Å)	Line
6562.44	0.05	V II
6563.51	0.15	Co I
6564.15	0.35	Unknown

Note. The first and second column define the spectral blends removed before applying the WFA: $\lambda_0 \pm \Delta\lambda$. The third column indicates the element of the transition if it is known.

of $B_{\rm LOS}$ inferred from applying the WFA to the Ca II 8542 Å and Hα data were estimated to be 23 and 18 G, respectively.

3.2. Milne–Eddington Inversion

We performed Milne–Eddington (ME) inversions (see chapter 11 of del Toro Iniesta 2007) of the Fe I 6569 Å data to infer the $B_{\rm LOS}$ (panel (f) of Figure 1) utilizing pyMilne code, a parallel C++/Python implementation[3] (de la Cruz Rodríguez 2019). The $B_{\rm LOS}$ from the Hα line is inferred from the WFA as explained in Section 3.1. The stratification of the $B_{\rm LOS}$ from the photosphere to the chromosphere is inferred using simultaneous multiline non-LTE inversions explained in Section 3.3.

3.3. Non-LTE Inversion

The MPI-parallel STockholm inversion Code (STiC, de la Cruz Rodríguez et al. 2016, 2019) is used to retrieve the stratification of atmospheric parameters. STiC is based on a modified version of the RH radiative transfer code (Uitenbroek 2001) and solves the polarized radiative transfer equation using cubic Bezier solvers (de la Cruz Rodríguez & Piskunov 2013). In non-LTE, assuming statistical equilibrium, it can fit multiple spectral lines simultaneously. It employs the fast approximation to account for partial redistribution effects (PRD; for more details Leenaarts et al. 2012b). STiC assumes plane-parallel geometry to fit the intensity in each pixel (also called the 1.5D approximation). STiC uses an LTE equation-of-state obtained from the library functions in the Spectroscopy Made Easy (SME) package code (Piskunov & Valenti 2017). The optical depth scale at 5000 Å (500 nm), abbreviated $\log\tau_{500}$, is used to stratify atmospheric parameters.

We have inverted the Stokes I and V profiles of the CaII 8542 Å, Si I 8536 Å, and Fe I 8538 Å lines simultaneously to infer the stratification of temperature (T), LOS velocity ($V_{\rm LOS}$), microturbulence ($V_{\rm turb}$), and LOS magnetic field ($B_{\rm LOS}$). We used a six-level Ca II atom. The Ca II H&K profiles were modeled in PRD (Milkey & Mihalas 1974; Uitenbroek 1989) and Ca II IR lines were synthesized in complete redistribution (CRD) approximation. The atomic parameters of the Si I 8536 Å and Fe I 8538 Å lines were obtained from the Vienna Atomic Line Database (VALD3; Ryabchikova et al. 2015) and Kurucz's line lists (Kurucz 2011), respectively, and synthesized under LTE approximation. The upper level of the Si I 8536 Å transition was treated with J_1-l (JK) coupling scheme as described in Appendix B. The latest version of the STiC inversion code has been upgraded to allow for the treatment of atomic levels of Kurucz's lines in JK coupling. An empirical loggf value of −1.4 was used for the Fe I 8538 Å transition (Socas-Navarro 2007).

[3] https://github.com/jaimedelacruz/pyMilne

Table 2
Node Positions ($\log\tau_{500}$ Scale) Used for Inversions of Different Categories of Profiles in T, $V_{\rm LOS}$, $V_{\rm turb}$, and $B_{\rm LOS}$

Parameters	Category	Cycle 1	Cycle 2
T	Quiescent	−5.5, −4,5, −3.5, −2.5, −1.5, 0	−5.5, −4.5, −3.5, −2.5, −1.5, 0
	Emission	−4.8, −3.8, −2.9, −1.8, −0.9, 0	−4.8, −3.8, −2.9, −1.8, −0.9, 0
$V_{\rm LOS}$	Quiescent	−4.5, −1	−4.5, −1
	Emission	−6, −4.5, −3, −1	−6, −4.5, −3, −1
$V_{\rm turb}$	All	−5, −4, −3, −1	−5, −4, −3, −1
$B_{\rm LOS}$	All	⋯	−4.5, −1

We used the k-means clustering to group the Stokes I profiles in different clusters such that similar-shaped profiles were grouped in one cluster. We then inverted the mean profile of each of those clusters to derive the stratification of T, $V_{\rm LOS}$, and $V_{\rm turb}$. Finally, the inferred stratification was used as the initial guess atmosphere to infer the stratification of the atmospheric parameters of the FOV, similar to the approach used by Nóbrega-Siverio et al. (2021) and Mathur et al. (2022). In the second cycle, we used the values of $B_{\rm LOS}$ derived from the ME inversions from the Fe I 6569 Å line and WFA of the Ca II 8542 Å line as the initial guess values of the $B_{\rm LOS}$ at $\log\tau_{500} = -1$ and −4.5, respectively. Earlier studies have found that the Stokes V profiles of the Ca II 8542 Å line have maximum response to the perturbations in the $B_{\rm LOS}$ between $\log\tau_{500} = -4$ and −5 (Quintero Noda et al. 2016a; Joshi & de la Cruz Rodríguez 2018; Murabito et al. 2019). Table 2 describes the node positions used for different categories of profiles. Quiescent profiles are nominal absorption profiles (910 profiles), and emission profiles are profiles that have an emission (or a hint of emission) in either blue or red or both the wings of the Ca II 8542 Å line (110 profiles). The quality of inversion fits are discussed in Appendix C.

We set the average velocity in the pore region in the photosphere ($\log\tau_{500}$ range of [−1, 0]) to rest for the absolute velocity calibration. With respect to the average profile in the pore, the quiet-Sun profile is blueshifted, that is, after velocity calibration, the $V_{\rm LOS}$ stratification inferred from the quiet-Sun profile shows an upflow of about $-3\ {\rm km\ s^{-1}}$.

4. Results and Discussion

4.1. Results from the WFA and ME Inversions

The $B_{\rm LOS}$ map inferred from the ME inversion of Stokes I and V profiles of Fe I 6569 Å line is shown in panel (f) of Figure 1. The maximum $B_{\rm LOS}$ strength found is +800 G. Panel (e) of Figure 1 shows the $B_{\rm LOS}$ map inferred from WFA applied on the Ca II 8542 Å within the wavelength range of $\lambda_0 \pm 0.25$ Å and the maximum $B_{\rm LOS}$ field strength found is +600 G. The region in the photosphere with opposite polarity of the $B_{\rm LOS}$ with respect to the pore has a field strength of about −200 G which is absent in the chromospheric $B_{\rm LOS}$ map.

4.2. Non-LTE Inversion Results

In this section, we discuss the results from the inversion of Stokes I and V profiles of the CaII 8542 Å, Si I 8536 Å, and Fe I 8538 Å lines using the STiC inversion code.

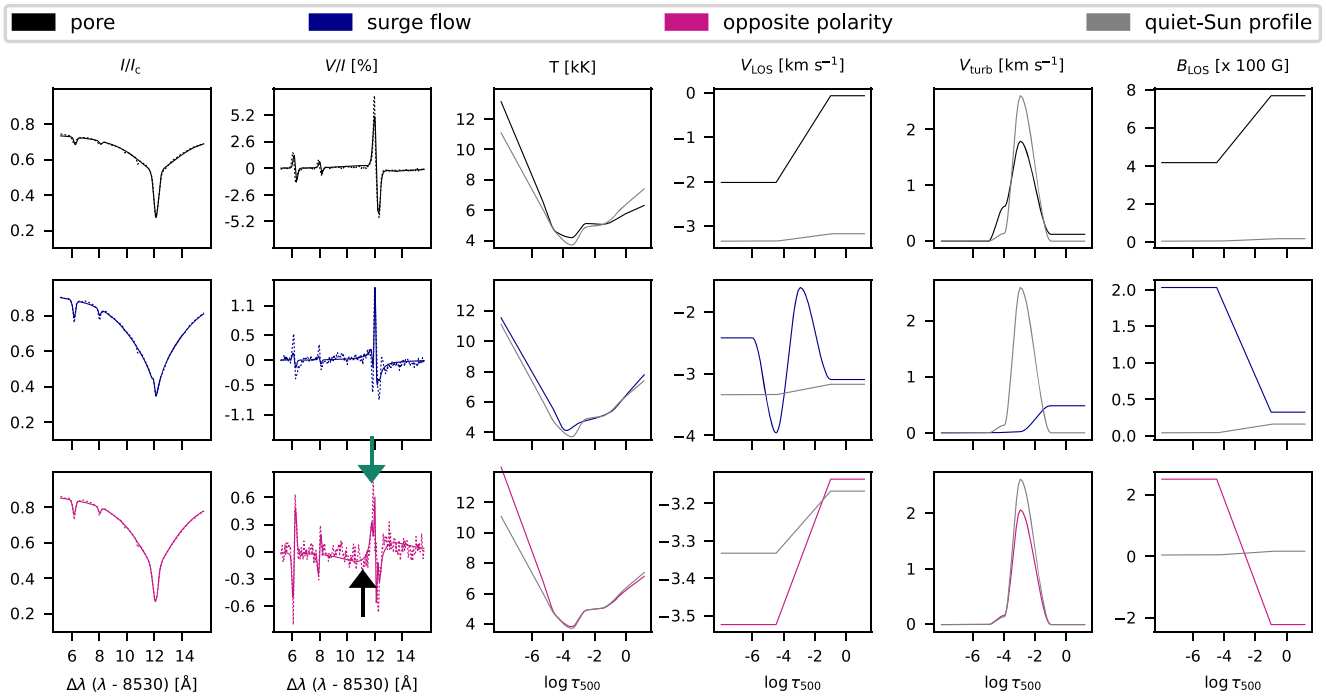

Figure 5. Inversion results of a few average profiles from different regions of the FOV. The dotted and dashed curves in the first two columns show the observed and fitted Stokes I and V profiles, respectively. The next three columns show the stratification of the T, $V_{\rm LOS}$, $V_{\rm turb}$, and $B_{\rm LOS}$ inferred from the inversions. The gray-colored curve shows the stratification of atmospheric parameters inferred from the inversions of an average quiet-Sun profile. The black and green arrows indicate the wavelength position in the wing and near the core of the Ca II 8542 Å line, respectively.

In Figure 5, we show inversion results of profiles averaged (to increase SNR) from a 3×3 box about the selected regions of the FOV, viz., pore, surge flow, and region with opposite polarity of the magnetic field. The average profile for the pore is calculated by averaging the pixels about the darkest pixel in the pore, for the surge flow profile by averaging about the blue-colored profile in Figure 2, and for the opposite polarity profile by averaging about the green colored profile in Figure 3.

The T stratification inferred from the pore profile has lower value of T at the photospheric layers ($\log \tau_{500} \sim -1$) and higher values at the chromospheric layers ($\log \tau_{500} \leqslant -4$) compared to that inferred from the inversion of the quiet-Sun profile. The $V_{\rm LOS}$ at photospheric layers ($\log \tau_{500} \sim -1$) is zero (calibrated) and at the chromospheric layers ($\log \tau_{500} = -4.5$) shows upflow of about $-2\,{\rm km\,s^{-1}}$. The $V_{\rm turb}$ is nonzero between $\log \tau_{500} = -1$ and -4. The value of $B_{\rm LOS}$ at the photospheric and chromospheric layers is about $+800$ G and $+400$ G, respectively.

The reversal of the sign of the Stokes V profile of the Ca II 8542 Å line shown in Figure 5 corresponding to surge flow region is a result of the emission feature in the blue wing of the Ca II 8542 Å line and is not an indication of any change in polarity of the $B_{\rm LOS}$. Accordingly, the T shows enhancement of about 600 K compared to T inferred from the quiet-Sun profile at $\log \tau_{500} = -4.5$ simultaneous with an upflow of about $-4\,{\rm km\,s^{-1}}$. For the pixels having spectral profiles similar to the surge flow, i.e., an emission feature in the blue wing and a red excursion in the Stokes I, the $V_{\rm turb}$ is small at all depth positions of $\log \tau_{500}$. It may be possible that such low values of $V_{\rm turb}$ may have some contribution in the higher temperature values inferred for the pixels in the surge flow region. Díaz Baso et al. (2022) have shown that there is a degeneracy between the T and the $V_{\rm turb}$. When the spectral profiles are in emission, the T and $V_{\rm turb}$ are anticorrelated; that is, an increase in T broadens the spectral line, and thus to maintain the same width, the $V_{\rm turb}$ must be decreased. However, the enhancement in T and minimal values of $V_{\rm turb}$ are necessary to achieve a satisfactory fit of the emission feature (for more discussion, see Mathur et al. 2022). The value of $B_{\rm LOS}$ at the photospheric and chromospheric layers is about $+50$ G and $+200$ G, respectively. The reason for the increased value of the magnetic field in the chromosphere compared to the photosphere is because the line core of the Ca II 8542 Å line is sampling the canopy fields overlying the pore and the nearby opposite polarity region.

The T, $V_{\rm LOS}$, and $V_{\rm turb}$ stratification inferred from the opposite polarity profile is similar to that inferred from the quiet-Sun profile. The value of $B_{\rm LOS}$ at the photospheric and chromospheric layers is about -220 G and $+250$ G, respectively, again suggesting a canopy structure.

As described in Section 2, above the positive polarity region, the sign of the Stokes V profile in the wings of the Ca II 8542 Å and Hα lines is opposite to that of in the core. This is probably because the line cores of the Hα and Ca II 8542 Å lines are sampling the canopy fields overlying the opposite polarity region. To verify that the wings and the core of the Ca II 8542 Å line are indeed sampling different layers of the atmosphere, in Figure 6, we show the response to perturbations of the $B_{\rm LOS}$ at one wavelength position in the wing ($\Delta\lambda = -1.03$ Å) and another one in the core ($\Delta\lambda = -0.11$ Å) of the line where the sign of the Stokes V is opposite. Beckers & Milkey (1975) define the response function (RF) for a physical parameter X as ${\rm RF}_X(\tau, \lambda) = \delta I(\lambda)/\delta X(\tau)$. Response functions contain information on how the Stokes parameters at different wavelength positions are sensitive to perturbations of a physical parameter at different $\log \tau_{500}$. The response function in the line wing of the Ca II 8542 Å line

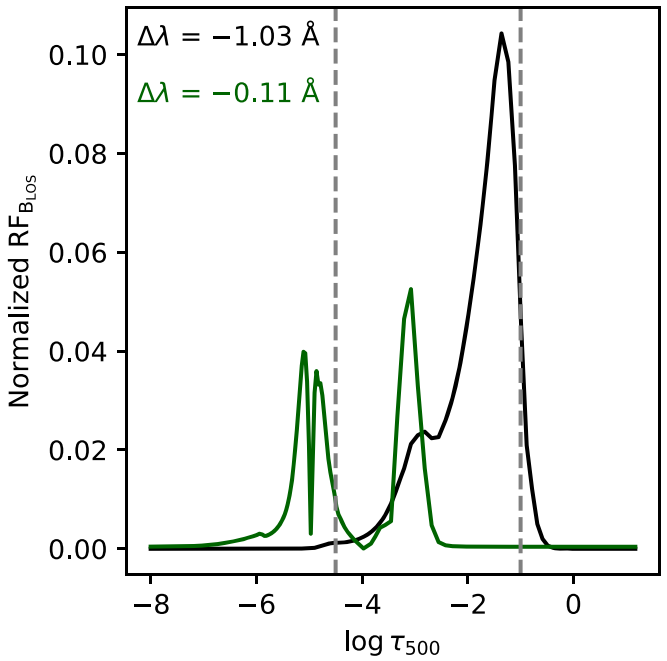

Figure 6. Normalized response function to the perturbations in the $B_{\rm LOS}$ at the wavelength positions $\Delta\lambda = -1.03$ and -0.11 Å (marked by black and green arrows in Figure 5) from the Ca II 8542 Å line core. The node positions for the $B_{\rm LOS}$ used in the inversions are represented by the vertical dashed gray lines.

shows a dominant contribution of the photospheric fields ($\log\tau_{500} \simeq -1.5$); in contrast, the response function near the line core shows a dominant contribution of the chromospheric fields ($\log\tau_{500} \leqslant -3$).

The maps of T, $V_{\rm LOS}$, and $V_{\rm turb}$ inferred from the inversions of the FOV at $\log\tau_{500} = -4.5$, -3, and -1 are presented in Figure 7. The morphological structure of the T map at $\log\tau_{500} = -1$ is similar to the far-wing image of the Ca II 8542 Å line (see panel (a) of Figure 1) with a decrease in T of about 300 K in the pore compared to surrounding background. There is a weak downflowing ($+2$ km s^{-1}) region near $(x, y) = (3\farcs5, 8\farcs8)$ while the rest of the pore does not show any signature of plasma flows. The value of $V_{\rm turb}$ is about 0–1 km s^{-1}in the $V_{\rm turb}$ maps at $\log\tau_{500} = -1$ except at a few regions where the $V_{\rm turb}$ is about 2–3 km s^{-1}such as the pore boundary ($6''$, $10\farcs8$).

The T at $\log\tau_{500} = -3$ ranges from 4 to 5.5 kK with a region of higher temperature ($T \sim 5.4$ kK) seen near the pore boundary ($6''$, $10\farcs8$). The temperature near the negative polarity region (in ME $B_{\rm LOS}$ map) is about 4.2 kK. The dark fibril-like lanes starting at ($2''$, $8\farcs8$), indicated by the ellipse-shaped contour in Figure 7, can also be seen in the Hα line core image (see panel (d) of Figure 1). The majority of the pore region shows upflows of up to -3 km s^{-1}. The $V_{\rm turb}$ inside the pore is about 0–3 km s^{-1}and outside the pore is about 3–5 km s^{-1}.

The morphological structure of the T map at $\log\tau_{500} = -4.5$ looks similar to the Ca II 8542 Å line core image (see panel (c) of Figure 1). The brightest and darkest pixels in panel (c) of Figure 1 correspond to T of about 5.7 kK and 3.8 kK, respectively. In general, the FOV show upflows of up to -3 km s^{-1} with two small regions showing downflows of about $+2$ km s^{-1}. The strong upflows up to -5 km s^{-1} are located in regions of higher temperature. There is almost zero $V_{\rm turb}$ in the $V_{\rm turb}$ map in all regions of the FOV.

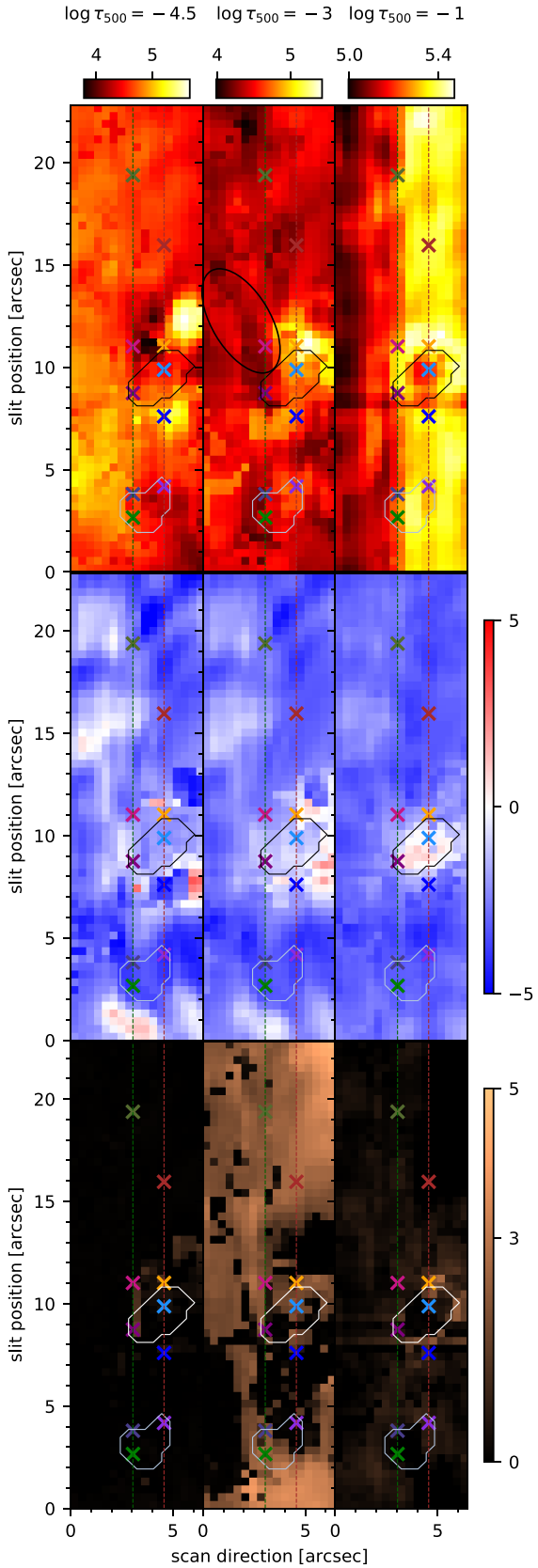

Figure 7. Maps of T, $V_{\rm LOS}$, and $V_{\rm turb}$ (row-wise) at $\log\tau_{500} = -4.5$, -3, -1 (column-wise) inferred from the inversions of the FOV. The contours, similar to Figure 1, show the location of the pore and the opposite polarity region. The slanted elliptical contour in the middle panel of the T maps show the location of the dark fibrillar region seen in the panel (d) of Figure 1.

Panels (a) and (b) of Figure 8 show maps of the magnetic field at $\log \tau_{500} = -1$ and -4.5. The change in the stratification of $|B_{\rm LOS}|$ inferred from inversions is shown in the middle panel of the bottom row of Figure 8. The morphological structure of the $B_{\rm LOS}$ map at the photospheric layers (at $\log \tau_{500} = -1$, panel (a) of Figure 8) is similar to panel (e) of Figure 1 with strong positive polarity in the pore ($\sim$+800 G) and nearby regions ($\sim$+350 G). An opposite polarity with a magnitude of $\sim$−200 G is seen in the $B_{\rm LOS}$ map. The field at $\log \tau_{500} = -4.5$ has positive polarity with a maximum $B_{\rm LOS}$ of $\sim$+600 G in the pore and about $\sim$+300 G in the opposite polarity region. In general, the structure of the $B_{\rm LOS}$ at $\log \tau_{500} = -4.5$ is more spread out compared to that of at $\log \tau_{500} = -1$ (see panel (b) of Figure 8). In addition, in the regions outside of the pore the $B_{\rm LOS}$ strength at $\log \tau_{500} = -4.5$ has increased compared to that at $\log \tau_{500} = -1$, suggesting a magnetic canopy-like structure (see middle panel in the bottom row of Figure 8). Using multiple spectral lines, the magnetic canopies around pores have also been reported by many authors in the recent literature (e.g., Keppens & Martinez Pillet 1996; Shimizu et al. 2012; Murabito et al. 2016; Buehler et al. 2019; Stauffer et al. 2022; Tapia & Bellot Rubio 2022). The magnetic field strengths inferred at $\log \tau_{500} = -1$ (the photosphere) and $\log \tau_{500} = -4.5$ (the chromosphere) are comparable with the values reported by many authors in recent literature, who studied the stratification of $B_{\rm LOS}$ in pores using spectral lines of the Fe I atom and Ca II 8542 Å and He I 10830 Å lines (Criscuoli et al. 2012; Sobotka et al. 2013; Jurčák et al. 2015; Quintero Noda et al. 2016b; Yadav et al. 2019; Nagaraju et al. 2020b; Sowmya et al. 2022).

4.3. Comparison of B_{LOS} Inferred from the Ca II 8542 Å and Hα Lines

Panels (c), (d), and (e) of Figure 8 show maps of the magnetic field inferred from the WFA method applied to the Stokes I and V profiles of the Hα line. The difference in amplitude of the $|B_{\rm LOS}|$ inferred from the Hα line with that inferred from the inversions is shown in the two rightmost panels of the bottom row of Figure 8. Figure 9 shows the scatterplots between the $|B_{\rm LOS}|$ inferred from inversions and the WFA.

The field strengths inferred from inversions of the Ca II 8542 Å line at $\log \tau_{500} = -4.5$ are comparable to those of inferred from the WFA of the Ca II 8542 Å line (see panel (a) of Figure 9), suggesting consistency between the two methods in inferring the $B_{\rm LOS}$. The magnetic field map inferred from the WFA of the Hα line core (Hα $\pm$ 0.35 Å) has a similar morphological structure to the map inferred from inversions of Ca II 8542 Å line at $\log \tau_{500} = -4.5$ (see panels (b) and (c) of Figure 8) suggesting the Hα line core probes the chromospheric magnetic field. The $B_{\rm LOS}$ field strength inferred from WFA of Hα line core is almost half (0.53 times) of that inferred from inversions at $\log \tau_{500} = -4.5$ and the WFA of the Ca II 8542 Å line (see the rightmost panel in the bottom row of Figure 8 and panel (b) and (c) of Figure 9). This could be due to sensitivity of the core of the Hα line to the magnetic field in the higher atmospheric layers than that of Ca II 8542 Å line. Or it could be due to systematic underestimation of $B_{\rm LOS}$ using the WFA from the Hα line. A detailed analysis of the Hα Stokes I and V profiles synthesized using current state-of-the-art model atmospheres of active regions and quiet Sun, taking into account the fine-structure sublevels (nlj) of the atomic levels (n), 3D radiative transfer, and the Zeeman effect, is required.

The maps of $B_{\rm LOS}$ inferred from the WFA method on the wings and the full spectral range of the Hα line show a morphological structure similar to that of $\log \tau_{500} = -1$ (see panel (d) and (e) of Figure 8), suggesting a significant contribution from the photospheric fields. However, the negative polarity region is not clearly seen. This is because, as explained in Section 2, there are very few spectral pixels with a clear signal of opposite sign in Stokes V profile in the line core and wings of the Hα line. The negative polarity region is very well reproduced through inversions because of good signal in Stokes V profiles of the Si I 8536 Å and Fe I 8538 Å lines. The $|B_{\rm LOS}|$ inferred from the full spectral range of the Hα line is weaker by a factor of 0.42 than that of $B_{\rm LOS}$ at $\log \tau_{500} = -1$, which is consistent with previous studies (see panel (d) of the Figure 9) (Abdussamatov 1971; Balasubramaniam et al. 2004; Hanaoka 2005; Nagaraju et al. 2008).

The above comparison of $B_{\rm LOS}$ inferred from the Hα and the Ca II 8542 Å lines suggest that the line core of the Hα line is sensitive to the chromospheric magnetic fields while the wings and the full Hα line exhibit significant sensitivity to the photospheric magnetic fields.

5. Conclusions

In this paper, we presented an analysis of spectropolarimetric observations recorded simultaneously in the Hα and Ca II 8542 Å lines of a pore with positive magnetic polarity, as well as the surrounding region that also covers a negative polarity magnetic field region. This is toward the goal of exploring the diagnostic potential of the Hα line to probe the chromospheric magnetic field. To estimate the $B_{\rm LOS}$ field from the Hα line, we have used the WFA, and from the Ca II 8542 Å line we have used both the WFA and inversion methods. The similarity between the magnetic field morphology inferred by applying the WFA on the core of the Hα and Ca II 8542 Å lines and inferred from inversions at $\log \tau_{500} = -4.5$ is clear evidence that the Hα line core probes the chromospheric magnetic field. This evidence is even more striking in the region above the negative polarity region in which the Hα and Ca II 8542 Å line cores exhibit positive polarity whereas the line wings exhibit negative polarity. This is because of the canopy fields from the dominant positive polarity region extended at the chromospheric heights overlying the negative polarity region, which is mostly confined to photospheric heights. It is found from the quantitative comparison that $B_{\rm LOS}$ fields estimated from the Hα line core are about $\approx$0.53 times that estimated from the Ca II 8542 Å line core. This may suggest that the magnetic sensitivity of the Hα line core is located in higher layers in the solar atmosphere than that of the Ca II 8542 Å line core. However, there is a possibility that $B_{\rm LOS}$ values are systematically underestimated from the Hα line under WFA. Further investigation through multiline spectropolarimetric observations and 3D radiative transfer calculations are required to fully understand the diagnostic potential of the Hα line to probe the chromospheric magnetic field.

We are grateful to the anonymous referee for their valuable feedback, which helped to enhance the quality of this manuscript. This research has made use of the High-Performance Computing (HPC) resources (NOVA cluster) made available by the Computer Center of the Indian Institute

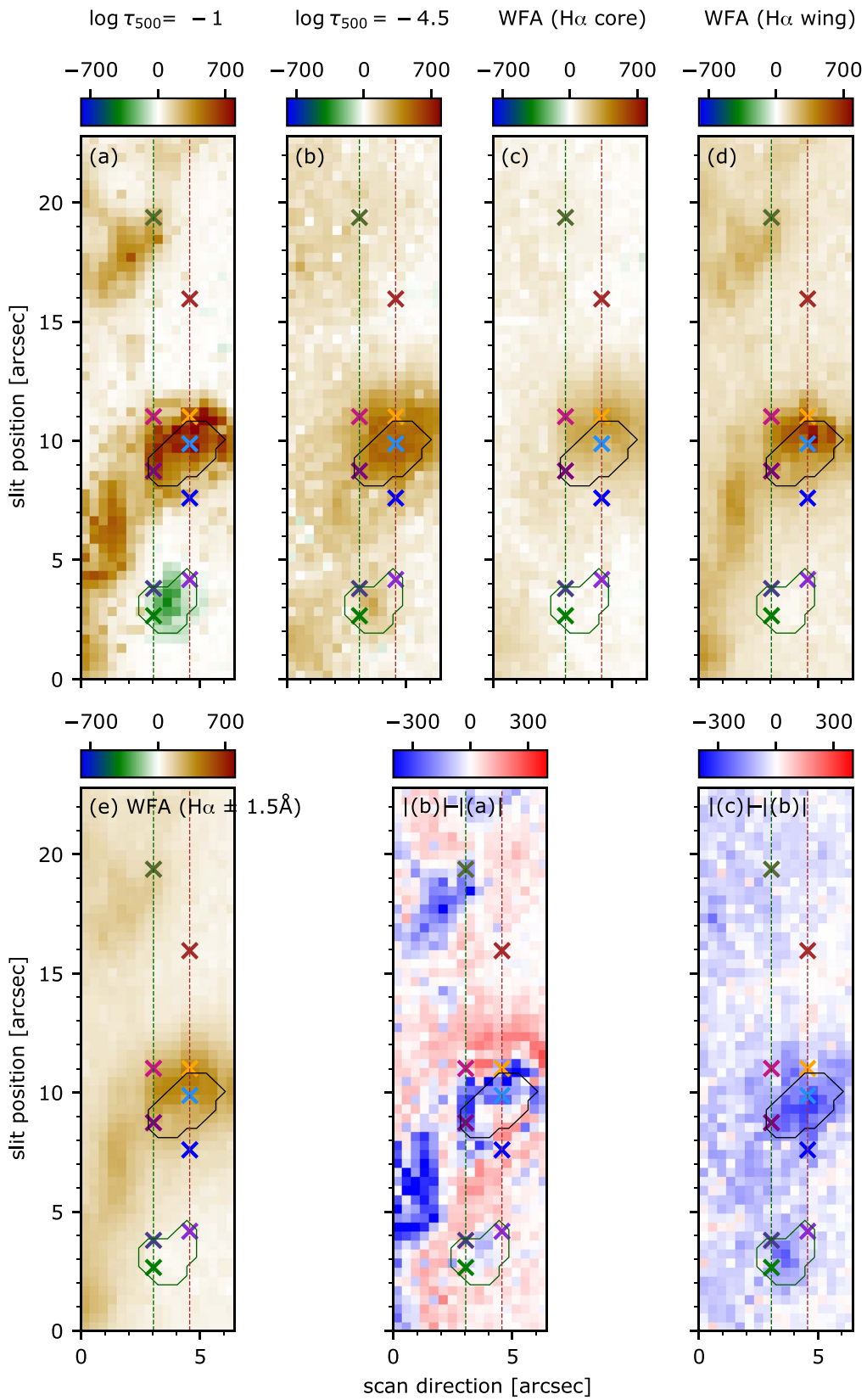

Figure 8. Maps of the $B_{\rm LOS}$ inferred from the inversions and the WFA. Panels (a) and (b) show the maps of $B_{\rm LOS}$ at $\log \tau_{500} = -1$ and -4.5, respectively. Panel (c) show the $B_{\rm LOS}$ inferred from the WFA of Hα spectral line in the spectral range ± 0.35 Å, panel (d) shows the WFA inferred from the wings of Hα spectral line in the range $[-1.5, -0.6]$ and $[+0.6, +1.5]$ Å, and panel (e) show the map of $B_{\rm LOS}$ from WFA inferred from Hα $\pm$ 1.5 Å. Change in the stratification of $|B_{\rm LOS}|$ is shown in the rightmost two panels of the bottom row as indicated on each panel. The black and green contours show the location of the pore and opposite polarity region, respectively.

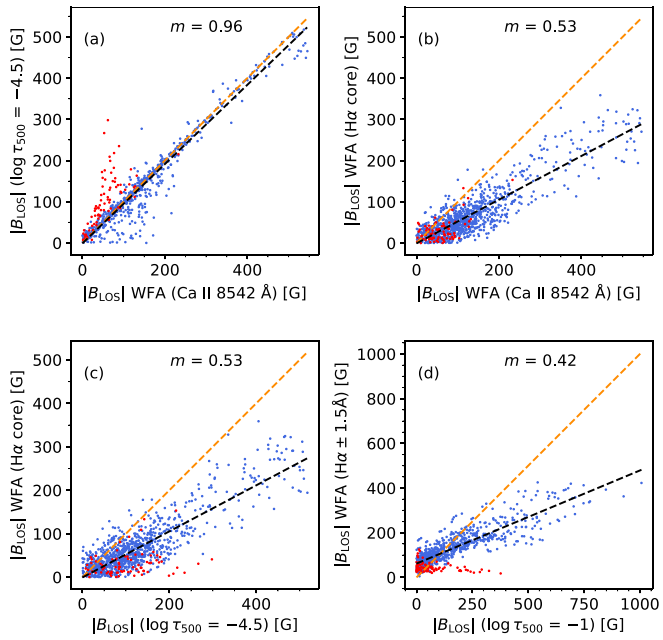

Figure 9. Comparison of the magnitude of $B_{\rm LOS}$ inferred from inversions and the WFA. The red and blue colors represent the pixels at photospheric layers with negative and positive polarity of the $B_{\rm LOS}$, respectively. Panel (a) shows the comparison between the $B_{\rm LOS}$ inferred at $\log \tau_{500} = -4.5$ with that inferred from WFA on the Ca II 8542 Å line. Panels (b) and (c) show the comparison between the $B_{\rm LOS}$ inferred by applying the WFA on the Hα line core with the $B_{\rm LOS}$ inferred from the WFA on Ca II 8542 Å line and at $\log \tau_{500} = -4.5$, respectively. Panel (d) shows the comparison between the $B_{\rm LOS}$ inferred by applying the WFA on the Hα $\pm$ 1.5 Å with $B_{\rm LOS}$ at $\log \tau_{500} = -1$. The black colored line shows the linear fit whose slope is indicated by m. The fiducial line is shown in yellow color for comparison.

of Astrophysics, Bangalore. This project has received funding from the European Research Council (ERC) under the European Union's Horizon 2020 research and innovation program (SUNMAG, grant agreement 759548). This work has made use of the VALD database, operated at Uppsala University, the Institute of Astronomy RAS in Moscow, and the University of Vienna. This research has made use of NASA's Astrophysics Data System Bibliographic Services. This research used version 3.1.6 (The SunPy Community et al. 2020) of the SunPy open source software package (Barnes et al. 2020). We have also used the packages h5py (Collette 2013), matplotlib (Hunter 2007), and numpy (Harris et al. 2020) to carry out our data analysis.

Facilities: SPINOR(DST).

Software: SunPy, NumPy, matplotlib, RH, STiC, pyMilne.

Appendix A
Data Reduction

The data are reduced with standard procedures of bias and flat-fielding. Calibration data with the procedures described in Socas-Navarro et al. (2006) are used to correct for instrumental polarization. No absolute wavelength calibration is done because of the absence of suitable telluric lines. Instead, we average a few spatial pixels in the quiescent region outside the pore (quiet-Sun profile) and fit the quiet-Sun profile over the full Ca II 8542 Å spectral range ($I_{\rm obs}^{\rm mean}$) with the BASS 2000 atlas (Paletou et al. 2009).

The procedures of the spectral veil correction, SI intensity calibration, and estimation of spectral Point-Spread Function (PSF) for the Ca II 8542 Å and Hα data are described as follows. We followed the spectral veil correction process described in Borrero et al. (2016) with an additional step correcting the tilt in the spectrum continuum. The continuum of the raw data, because of detector flat-field residuals and pre-filter shape, is tilted. These tilts were corrected in the data reduction pipeline by subtracting a linear fit ($y = a + b\ \lambda$) with the average spectrum. However, the observed spectral range is not symmetric with respect to the core of the Ca II 8542 Å and Hα lines, and there is an inherent tilt present even in the BASS 2000 atlas. Hence we again corrected this over-correction in the tilts by dividing with a normalized linear fit by matching the continuum intensity levels to that of the reference profile ($I_{\rm ref}$). For the Ca II 8542 Å data, we used spectra synthesized using the RH code (Uitenbroek 2001) with FAL-C (Avrett 1985; Fontenla et al. 1993) model atmosphere at $\mu = 0.8$ as $I_{\rm ref}$. We ensured that there is a good match of synthesized spectra of the Ca II 8542 Å line at $\mu = 1$ with BASS 2000 atlas spectrum, which gave us confidence in using $\mu = 0.8$ spectra as $I_{\rm ref}$. After correcting the continua tilt, we estimated the PSF and stray-light fraction. PSF is assumed to be Gaussian (σ) for the whole Ca II 8542 Å line spectral range, but stray-light fraction (ν) is allowed to vary over the blends of the Si I 8536 Å, the Fe I 8538 Å, and about the Ca II 8542 Å line core. To estimate σ and ν, we minimized the χ^2 distance between the $I_{\rm obs}^{\rm mean}$ and $I_{\rm ref}^{\rm degraded}$ with σ and ν

$$I_{\rm ref}^{\rm degraded}(\lambda) = (1 - \nu) I_{\rm ref}(\lambda) \ * \ g(\lambda, \sigma) + \nu \ * \ I_{\rm ref}^{\rm c}(\lambda) \tag{A1}$$

where $I_{\rm ref}^{\rm c}$ is the value of intensity at the observed predefined far-wing wavelength point. The absolute SI intensity calibration is done by comparing the intensity of the observed predefined continuum wavelength point with the intensity at degraded $I_{\rm ref}$.

We followed a similar process for estimation of the spectral veil and spectral PSF for the Hα data, but instead of using synthesized spectrum as $I_{\rm ref}$, we inferred $I_{\rm ref}$ using BASS 2000 atlas Hα spectrum (Paletou et al. 2009) and center-to-limb variation calculated from $\mu = 1$ to $\mu = 0.8$ using the RH code with FAL-C model atmosphere. We used a six-level hydrogen atom without a fine structure to synthesize the intensity of Hα line with the blend of the Fe I 6569 Å line. The atomic parameters of the Fe I 6569 Å line are retrieved from Kurucz's line lists (Kurucz 2011) and synthesized in LTE approximation.

Appendix B
JK Coupling

In J_1-l (JK) coupling scheme, a "parent" level of orbital angular momentum L_1 and spin S_1 couples its total angular momentum J_1 with the orbital angular momentum l of a further electron, to give an angular momentum K, which in turn couples with the electron's spin to give total angular momentum J (for more details, see page 77 of Landi Degl'Innocenti & Landolfi 2004).

The Landé factor for level in J_1-l (JK) coupling is

$$g_{J_1-l} = 1 + \gamma(J, 1/2, K) + \gamma(J, K, 1/2)\gamma(K, J_1, l)\gamma \times (J_1, S_1, L_1) \tag{B1}$$

where

$$\gamma(A, B, C) = \frac{A(A+1) + B(B+1) - C(C+1)}{2A(A+1)}. \quad \text{(B2)}$$

Appendix C
Quality of Fits

In Figure 10, we discuss the match between the observed and synthesized Stokes I and V for the profiles discussed in the paper.

In general, the synthesized Stokes I and V profiles show a good match with the observed profiles. The emission in the blue wing of the Ca II 8542 Å line and reversal in the Stokes V is very well reproduced in the synthesized profiles (see blue-colored profile). When the Stokes V signal is higher than 1%, a good match is seen in the Si I 8536 Å, Fe I 8538 Å, and Ca II 8542 Å Stokes I and V profiles, for example, cyan-, maroon-, pink-, and khaki-colored profiles. The opposite sign is very well reproduced in the Stokes V signal of the Si I 8536 Å and Fe I 8538 Å lines and reversal in the Ca II 8542 Å line far-wing Stokes V signal, for example, green- and purple-colored profiles. When the signal in Stokes V is less than 0.5%, the match of the synthesized Stokes V profile is relatively poor compared to the above cases, for example, purple- and brown-colored profiles.

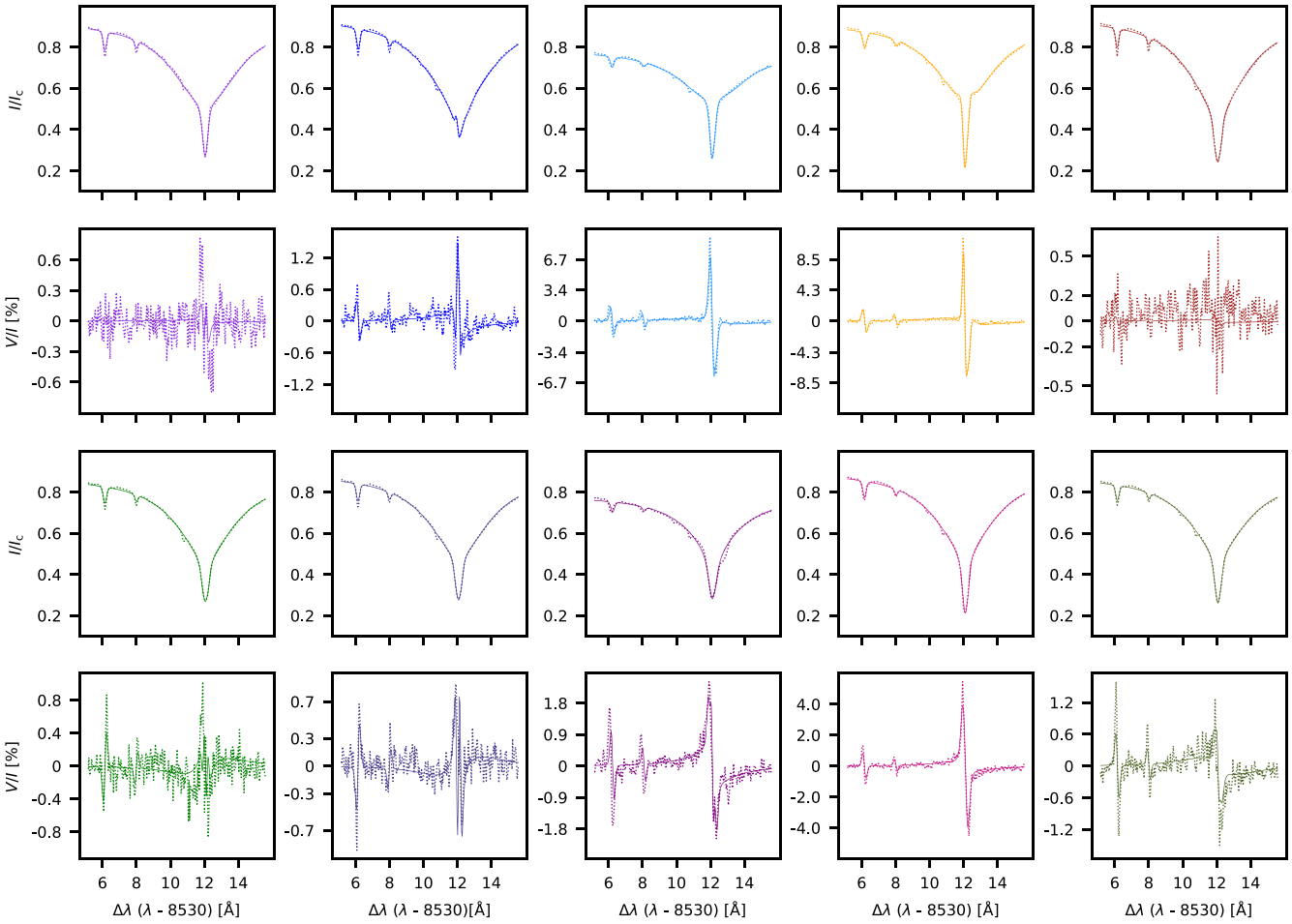

Figure 10. Examples of the observed (dotted lines) and synthesized (solid lines) Ca II 8542 Å Stokes I and V profiles for the pixels marked by x in Figure 1.

ORCID iDs

Harsh Mathur https://orcid.org/0000-0001-5253-4213
K. Nagaraju https://orcid.org/0000-0002-0465-8032
Jayant Joshi https://orcid.org/0000-0003-0585-7030
Jaime de la Cruz Rodríguez https://orcid.org/0000-0002-4640-5658

References

Abdussamatov, H. I. 1971, SoPh, 16, 384
Andretta, V., & Jones, H. P. 1997, ApJ, 489, 375
Asensio Ramos, A., Trujillo Bueno, J., & Landi Degl'Innocenti, E. 2008, ApJ, 683, 542
Avrett, E. H. 1985, in Chromospheric Diagnostics and Modelling, Proc. of the Conf., ed. B. W. Lites (Sunspot, NM: National Solar Observatory), 67
Balasubramaniam, K. S., Christopoulou, E. B., & Uitenbroek, H. 2004, ApJ, 606, 1233
Barnes, W. T., Bobra, M. G., Christe, S. D., et al. 2020, ApJ, 890, 68
Beckers, J. M., & Milkey, R. W. 1975, SoPh, 43, 289
Bjørgen, J. P., Leenaarts, J., Rempel, M., et al. 2019, A&A, 631, A33
Borrero, J. M., Asensio Ramos, A., Collados, M., et al. 2016, A&A, 596, A2
Buehler, D., Lagg, A., van Noort, M., & Solanki, S. K. 2019, A&A, 630, A86
Carlsson, M., & Stein, R. F. 2002, ApJ, 572, 626
Casini, R., & Landi Degl'Innocenti, E. 1994, A&A, 291, 668
Collette, A. 2013, Python and HDF5 (Sebastopol, CA: O'Reilly & Associates)
Criscuoli, S., Del Moro, D., Giannattasio, F., et al. 2012, A&A, 546, A26
de la Cruz Rodríguez, J. 2019, A&A, 631, A153
de la Cruz Rodríguez, J., Leenaarts, J., & Asensio Ramos, A. 2016, ApJL, 830, L30
de la Cruz Rodríguez, J., Leenaarts, J., Danilovic, S., & Uitenbroek, H. 2019, A&A, 623, A74
de la Cruz Rodríguez, J., & Piskunov, N. 2013, ApJ, 764, 33
del Toro Iniesta, J. C. 2007, Introduction to Spectropolarimetry (Cambridge: Cambridge Univ. Press)
Díaz Baso, C. J., Asensio Ramos, A., & de la Cruz Rodríguez, J. 2022, A&A, 659, A165
Dunn, R. B. 1969, S&T, 38, 368
Fontenla, J. M., Avrett, E. H., & Loeser, R. 1993, ApJ, 406, 319
Hanaoka, Y. 2005, PASJ, 57, 235
Harris, C. R., Millman, K. J., van der Walt, S. J., et al. 2020, Natur, 585, 357
Hunter, J. D. 2007, CSE, 9, 90
Jaume Bestard, J., Trujillo Bueno, J., Bianda, M., Štěpán, J., & Ramelli, R. 2022, A&A, 659, A179
Joshi, J., & de la Cruz Rodríguez, J. 2018, A&A, 619, A63
Jurčák, J., Bello González, N., Schlichenmaier, R., & Rezaei, R. 2015, A&A, 580, L1
Keppens, R., & Martinez Pillet, V. 1996, A&A, 316, 229
Kerr, G. S., Fletcher, L., Russell, A. J. B., & Allred, J. C. 2016, ApJ, 827, 101
Kuridze, D., Henriques, V. M. J., Mathioudakis, M., et al. 2018, ApJ, 860, 10
Kurucz, R. L. 2011, CaJPh, 89, 417
Lagg, A., Lites, B., Harvey, J., Gosain, S., & Centeno, R. 2017, SSRv, 210, 37
Landi Degl'Innocenti, E., & Landolfi, M. 2004, Polarization in Spectral Lines, Vol. 307 (Dordrecht: Kluwer)
Leenaarts, J., Carlsson, M., & Rouppe van der Voort, L. 2012a, ApJ, 749, 136
Leenaarts, J., Pereira, T., & Uitenbroek, H. 2012b, A&A, 543, A109
Leenaarts, J., Golding, T., Carlsson, M., Libbrecht, T., & Joshi, J. 2016, A&A, 594, A104
López Ariste, A., Casini, R., Paletou, F., et al. 2005, ApJL, 621, L145
Martínez González, M. J., & Bellot Rubio, L. R. 2009, ApJ, 700, 1391
Mathur, H., Joshi, J., Nagaraju, K., van der Voort, L. R., & Bose, S. 2022, A&A, 668, A153
Milkey, R. W., & Mihalas, D. 1974, ApJ, 192, 769
Murabito, M., Ermolli, I., Giorgi, F., et al. 2019, ApJ, 873, 126
Murabito, M., Romano, P., Guglielmino, S. L., Zuccarello, F., & Solanki, S. K. 2016, ApJ, 825, 75
Nagaraju, K., Sankarasubramanian, K., & Rangarajan, K. E. 2008, ApJ, 678, 531
Nagaraju, K., Sankarasubramanian, K., & Rangarajan, K. E. 2020a, JApA, 41, 10
Nagaraju, K., Sankarasubramanian, K., & Rangarajan, K. E. 2020b, in IAU Symp. 354, Solar and Stellar Magnetic Fields: Origins and Manifestations, ed. A. Kosovichev, S. Strassmeier, & M. Jardine (Cambridge: Cambridge Univ. Press), 46
Nóbrega-Siverio, D., Guglielmino, S. L., & Sainz Dalda, A. 2021, A&A, 655, A28
Paletou, F., Lafon, M., Maeght, P., et al. 2009, in ASP Conf. Ser. 405, Solar Polarization 5: In Honor of Jan Stenflo, ed. S. V. Berdyugina, K. N. Nagendra, & R. Ramelli (San Francisco, CA: ASP), 397
Piskunov, N., & Valenti, J. A. 2017, A&A, 597, A16
Quintero Noda, C., Shimizu, T., de la Cruz Rodríguez, J., et al. 2016a, MNRAS, 459, 3363
Quintero Noda, C., Shimizu, T., Ruiz Cobo, B., et al. 2016b, MNRAS, 460, 1476
Rimmele, T. R. 2000, Proc. SPIE, 4007, 218
Ruiz Cobo, B., Quintero Noda, C., Gafeira, R., et al. 2022, A&A, 660, A37
Ryabchikova, T., Piskunov, N., Kurucz, R. L., et al. 2015, PhyS, 90, 054005
Sanchez Almeida, J. 1997, A&A, 324, 763
Sankarasubramanian, K., & Rimmele, T. 2002, ApJ, 576, 1048
Shimizu, T., Ichimoto, K., & Suematsu, Y. 2012, ApJL, 747, L18
Sobotka, M., Švanda, M., Jurčák, J., et al. 2013, A&A, 560, A84
Socas-Navarro, H. 2007, ApJS, 169, 439
Socas-Navarro, H., Elmore, D., Pietarila, A., et al. 2006, SoPh, 235, 55
Socas-Navarro, H., Trujillo Bueno, J., & Ruiz Cobo, B. 2000a, ApJ, 530, 977
Socas-Navarro, H., Trujillo Bueno, J., & Ruiz Cobo, B. 2000b, ApJ, 544, 1141
Socas-Navarro, H., & Uitenbroek, H. 2004, ApJL, 603, L129
Sowmya, K., Lagg, A., Solanki, S. K., & Castellanos Durán, J. S. 2022, A&A, 661, A122
Stauffer, J. R., Reardon, K. P., & Penn, M. 2022, ApJ, 930, 87
Štěpán, J., & Trujillo Bueno, J. 2010, MmSAI, 81, 810
Štěpán, J., & Trujillo Bueno, J. 2011, ApJ, 732, 80
Tapia, A. S., & Bellot Rubio, L. R. 2022, in 44th COSPAR Scientific Assembly (Paris: COSPAR), 2512
The SunPy Community, Barnes, W. T., Bobra, M. G., et al. 2020, ApJ, 890, 68
Uitenbroek, H. 1989, A&A, 213, 360
Uitenbroek, H. 2001, ApJ, 557, 389
Yadav, R., de la Cruz Rodríguez, J., Díaz Baso, C. J., et al. 2019, A&A, 632, A112